DOI: https://doi.org/10.1063/5.0231467

Publisher: AIP Publishing

Version: Accepted Version

Coupling analysis between wave resonance in the moonpool and heave motion of the twin hulls with mooring effect

Sheng-Chao Jiang (姜胜超)[a,*], Jun-Jie Lan (兰俊杰)[b,a], Wei Bai (柏威)[c], Yong-Qiang Huang (黄永强)[d,a]

[a]*School of Naval Architecture, Dalian University of Technology, Dalian 116024, China*
[b]*Power China Huadong Engineering Corporation Limited, Hangzhou, 311122, China*
[c]*Department of Computing and Mathematics, Manchester Metropolitan University, Chester Street, Manchester M1 5GD, UK*
[d]*Dalian Shipbuilding Industry Co., Ltd, 116024, China*

Abstract

Fluid resonance in the moonpool formed by two identical rectangular hulls in water waves is investigated by employing the Computational Fluid Dynamics (CFD) package OpenFOAM®. The influence of the vertical stiffness on the behavior of the moonpool resonance coupling with the heave motion response is presented. Numerical simulations show that the free surface oscillation in the moonpool exhibits a two-peak variation with the incident wave frequency, defined as the first and second peak frequencies. A local Keulegan-Carpenter (KC) number is introduced for describing the influence of the fluid viscosity and flow rotation on the fluid resonance and heave motion resonance. At the first peak frequency, the free surface oscillation and heave motion response show an in-phase relationship, where the increase of the vertical stiffness can increase the relative motion between them. This finally leads to an increase in the KC number, indicating the increased effect of the energy dissipation with the increase of the vertical stiffness. At the second peak frequency with an out-of-phase relationship between the free surface oscillation and heave motion response, the variation of the KC number is not sensitive to the vertical stiffness. Correspondingly, the influence of the energy dissipation is not much dependent on the vertical stiffness.

Keywords: Wave resonance, Moonpool, Heave motion, KC Number, Energy dissipation, Mooring effect

1. Introduction

Moonpool is a vertical opening through the deck and hull of ships or barges, which can be used to carry out marine operations such as pipe laying or diver recovery. The riser system also passes through a moonpool in offshore structures, such as drilling ships, Spar platforms, Floating Liquefied Natural Gas (FLNG) and Floating Production Storage and Offloading (FPSO) systems. In practical engineering, careful design is required in order to avoid excessive free surface resonance in the moonpool and the associated motion response of the floater. Therefore, an in-depth understanding of the fundamental physics of the fluid resonance in the moonpool is essential for marine operation and structure safety.

*Corresponding author
Email address: jiangshengcaho@foxmail.com (Sheng-Chao Jiang (姜胜超))

Faltinsen et al. (2007) and Molin et al. (2018) derived a semi-analytical solution for the fluid resonance in the moonpool, where the piston- and sloshing-mode resonances were formulated and solved via an approximate eigenvalue problem. Sun et al. (2010) and Feng and Bai (2015) simulated the free surface resonance in the moonpool between two barges in a side-by-side arrangement by using the second-order and fully nonlinear potential flow models, respectively. However, the application of the potential flow model was reported to over-predict the free surface amplitude around resonant frequencies, which is attributed to the absence of fluid viscosity and flow rotation. This has been extensively confirmed by experimental measurements, such as Saitoh et al. (2006), Iwata et al. (2007) and Zhao et al. (2017b), among others. To resolve this problem, Newman (2004) and Chen (2004) adopted an improved potential flow model based on the introduction of artificial damping to suppress the exaggerated resonant amplitudes. The keys of this method are the formulation of the damping term and the selection of the damping coefficient, where many efforts have been devoted to (Lu et al., 2011a,b; Liu and Li, 2014; Feng et al., 2018; Tan et al., 2019, 2021). Another alternative method is Computational Fluid Dynamics (CFD) simulations based on the Navier-Stokes solvers, which has become more popular with the development of numerical and computing techniques (Lu et al., 2010; Fredriksen et al., 2014; Moradi et al., 2015; Jiang et al., 2018; Gao et al., 2019; Wang et al., 2019). The CFD methods are able to capture the energy dissipation caused by the fluid viscosity and flow rotation, which are closely dependent on the numerical scheme and the mesh density.

The above work mainly considered the fluid resonance in the moonpool under wave diffraction or radiation scenarios. That is, these studies only focused on the free surface oscillation in the moonpool between either fixed hulls in water waves or hulls undergoing forced motions in the still water. However, it is an interaction problem between the incident water wave and the floating bodies in practical engineering. Fredriksen et al. (2015) and Ravinthrakumar et al. (2020) measured the fluid resonance in the moonpool coupling with the motion response of the floater. Zhang et al. (2022) conducted laboratory tests of the coupling effect on the free surface oscillation for a sway-box section adjacent to a fixed structure. In addition to experimental measurements, numerical simulations are also effective tools for this topic. Li and Teng (2021) simulated the free surface oscillation in the moonpool formed by twin-floating barges with the roll motion response under wave actions. Gao et al. (2021, 2024) studied the influence of heave motion response on the fluid resonance in the moonpool in regular and irregular waves. Jing et al. (2023, 2024) simulated the roll motion effect on the wave resonance in the moonpool induced by higher-order harmonic components of incident waves. According to the laboratory tests and numerical simulations, the significant effect of motion response on the behavior of fluid resonance in the moonpool can be confirmed.

In addition, the mooring stiffness plays an important role in the behavior of floaters in practical engineering, which may further affect the coupling actions between the fluid resonance in the moonpool and the motion response of the floater. However, to the best of the authors' knowledge, very few studies have been paid on this topic, and the only relevant study is found in Lu et al. (2020) for the fluid resonance in the narrow gap formed by a box-wall system, where the heave and sway responses of the box section with different mooring stiffnesses were investigated. Moreover, as mentioned above, the energy dissipation associated with the fluid viscosity and flow rotation significantly affects the behavior of fluid resonance in the moonpool. A further understanding of the influence of energy dissipation during the coupling actions between the fluid resonance and the motion response of the moored floater is expected. In this paper, numerical simulations are carried out for the fluid resonance in the moonpool formed by the free-heave twin hulls coupling with the vertical stiffness effect. The influence of vertical stiffness on the behaviour of coupling actions is the major contribution of this study to offshore engineering. In collaboration with the quantitative description of the local Keulegan-Carpenter (KC) number and the examination of vortex shedding in the flow patterns, the energy dissipation during the coupling process with various mooring stiffnesses is revealed, which highlights the academic contribution of this study.

2. Mathematical formulation

Two numerical models, that is, the potential flow model and the viscous fluid flow model, are adopted to carry out the investigations in this study. The potential flow model is efficient, so it is used for the general description of the behaviour of the heave motion response and the free surface oscillation. However, it cannot capture the realistic physical phenomena around the peak frequencies due to the ignorance of the fluid viscosity and flow rotation. Therefore, the viscous fluid flow model is employed for the detailed analysis of the coupling actions between the heave motion and the fluid resonance. The model details are provided below.

2.1. Viscous fluid flow model

The Navier-Stokes equations for two-phase incompressible turbulent flows in the Arbitrary Lagrangian-Eulerian (ALE) reference system are adopted as the governing equations,

$$\frac{\partial \rho}{\partial t} + \frac{\partial \rho u_i}{\partial x_i} = 0, \tag{1a}$$

$$\frac{\partial \rho u_i}{\partial t} + \frac{\partial \rho (u_j - u_j^m) u_i}{\partial x_j} = \rho g_i - \frac{\partial p}{\partial x_i} + \mu_e \frac{\partial}{\partial x_j}\left(\frac{\partial u_i}{\partial x_j} + \frac{\partial u_j}{\partial x_i}\right), \tag{1b}$$

where x_i and u_i are the Cartesian coordinate component and the fluid velocity component in the ith direction, respectively; u_i^m is the velocity component due to mesh deformation in the ALE frame. g_i is the gravitational acceleration; p is the fluid pressure. ρ and μ_e are the fluid density and effective dynamic viscosity, respectively. $\mu_e = \mu_m + \mu_t$, where μ_m is the fluid molecule viscosity and μ_t is the turbulent viscosity.

The Re-Normalization Group (RNG) $k-\varepsilon$ two-equation formulations are selected for closing the governing equations,

$$\mu_t = C_\mu \frac{k^2}{\varepsilon}, \tag{2}$$

where $C_\mu = 0.09$ is a theoretical model constant, and the time-dependent advection-diffusion equations for the turbulent kinematic energy k and its dissipation rate ε can be written as,

$$\frac{\partial \rho k}{\partial t} + \frac{\partial \rho (u_j - u_j^m) k}{\partial x_j} = \frac{\partial}{\partial x_j}\left(\frac{\mu_t}{\sigma_k}\frac{\partial k}{\partial x_j}\right) + \mu_t \left(\frac{\partial u_i}{\partial x_j} + \frac{\partial u_j}{\partial x_i}\right)\frac{\partial u_i}{\partial x_j} - \rho\varepsilon, \tag{3a}$$

$$\frac{\partial \rho \varepsilon}{\partial t} + \frac{\partial \rho (u_j - u_j^m) \varepsilon}{\partial x_j} = \frac{\partial}{\partial x_j}\left(\frac{\mu_t}{\sigma_\varepsilon}\frac{\partial \varepsilon}{\partial x_j}\right) + C_{1\varepsilon}\frac{\varepsilon}{k}\mu_t \left(\frac{\partial u_i}{\partial x_j} + \frac{\partial u_j}{\partial x_i}\right)\frac{\partial u_i}{\partial x_j} - \rho C_{2\varepsilon}\frac{\varepsilon^2}{k}, \tag{3b}$$

where the model constants $C_{1\varepsilon}$, $C_{2\varepsilon}$, σ_k and σ_ε are 1.42, 1.68, 0.71942 and 0.71942, respectively. They were derived theoretically in the RNG turbulent model (Yakhot and Orszag, 1986; Yakhot and Smith, 1992).

The Volume of Fluid (VOF) method is adopted to track the fluid and capture the free surface motion. In the method, the fraction indicator α is defined as 0 for air and 1 for water, and any intermediate value between 0 and 1 represents a mixture of air and water. The distribution of α satisfies the following advection equation,

$$\frac{\partial \alpha}{\partial t} + (u_i - u_i^m)\frac{\partial \alpha}{\partial x_i} = 0. \tag{4}$$

The spatial variation of fluid density and dynamic viscosity can be obtained according to the fraction indicator α in the computational cell as follows,

$$\rho = \alpha \rho_W + (1-\alpha)\rho_A, \tag{5a}$$

$$\mu = \alpha \mu_W + (1-\alpha)\mu_A, \tag{5b}$$

where the subscripts W and A represent the Water phase and Air phase, respectively. In numerical simulations, the contour with $\alpha = 0.50$ is used to represent the interface between the water and air phases.

The toolbox 'waves2Foam' proposed by Jacobsen et al. (2012) is utilized to generate the incident wave and avoid the internal wave reflection, where relaxation zones are defined at the inlet and outlet boundaries of the numerical wave flume. The exponential relaxation function,

$$\phi_R(\chi_R) = 1 - \frac{\exp(\chi_R^{3.5}) - 1}{\exp(1) - 1}, \qquad \chi_R \in [0, 1], \tag{6}$$

is applied within the relaxation zone,

$$\vartheta = \phi_R \vartheta_C + (1 - \phi_R)\vartheta_T, \tag{7}$$

where ϑ is either the velocity u_i or the fraction indicator of water α, and the subscripts C and T represent the Computed value and Target value, respectively.

The simulations are conducted in the Supercomputer Center of Dalian University of Technology by using the OpenFOAM® package with version 3.0.0. The initial condition in the numerical computations is the still state, which is the zero velocity and hydrostatic pressure in the numerical wave flume. The no-slip boundary condition is imposed at the solid wall including the hull surface and seabed. At the upper boundary of the numerical wave flume, the Dirichlet and Neumann types of boundary conditions are prescribed for the pressure and velocity respectively. An incident fifth-order Stokes wave is adopted at the inlet boundary, where the gradient of pressure is set to zero. The governing equations (1a)-(1b) and the advection transport equation (4) are solved based on the Finite Volume Method (FVM). The velocity and pressure are decoupled by the PISO (Pressure Implicit with Splitting of Operators) algorithm (Issa, 1986). The time increment is determined automatically according to the Courant-Friedrichs-Lewy (CFL) condition, where the largest allowed Courant Number is set to $C_r = 0.20$.

2.2. Potential flow model

The classical linear potential flow model is also adopted in this study for the purpose of comparison. The boundary integral equation based on the Rankine source $G(\mathbf{x}, \mathbf{x_0}) = \frac{1}{2\pi}(\ln r + \ln r')$ is established, which has been described in the previous work in Jiang et al. (2017). The higher-order boundary element method (HOBEM) with quadratic isoparameteric elements (Teng and Eatock Taylor, 1995) is employed to discrete the boundary integral equation. The detailed theoretical formulation is omitted here, as it is well-known in many textbooks.

3. Mesh convergence and numerical validation

The wave interaction with two identical free-heave hulls with a moonpool in the centre is investigated in this study, as shown in Fig. 1. The large-amplitude piston-type free surface oscillation in the moonpool is focused, which is one of the most important issues in the coupling analysis. The hulls of breadth B_L and height B_H with the moonpool of draft D and breadth B_{mp} are situated in a numerical wave flume with the water depth h. In this study, the twin hulls are rigidly connected and only the heave motion is free. Two relaxation zones are situated on the left and right sides of the numerical wave flume, respectively, where the lengths of the zones are generally about 1.5 - 2.0 times the wavelength λ in the numerical simulations. A total of four wave gauges are equipped to record the free surface elevations. G2 and G3 with a distance of 0.25 λ between them are situated 1.5 λ from the left side of the hulls for separating the incident and reflected waves; while G4 located 1.5 λ from the right side of the hulls is adopted for measuring the transmission wave. The wave gauge G1 is situated in the middle of the moonpool for recording the free surface oscillation in the moonpool. Numerical simulations have confirmed that there is no sloshing-type free surface oscillation in this study. Finally, it should be noted that all of the free surface amplitudes in this work are calculated in the *space-fixed coordinate system*.

Numerical simulations begin from the mesh convergent test in this study, where the geometries of the twin hulls with a moonpool are $B_L = 0.360$ m, $B_H = 0.360$ m, $B_{mp} = 0.180$ m and $D = 0.180$ m. The water depth of the numerical wave flume is $h = 1.030$ m and the incident wave height is $H_i = 0.03$ m, where the relationship between the wave height and wave amplitude is $H_i = 2A_i$. The non-uniform meshes are adopted to minimize the number of meshes and save computational resources. In general, the square fine

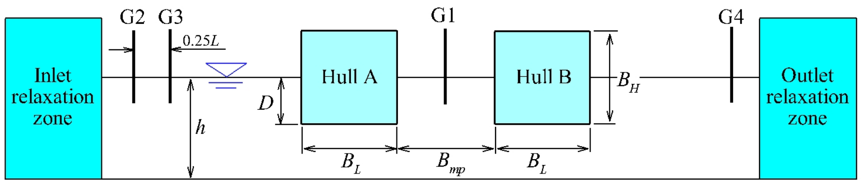

Figure 1: Sketch of the numerical wave flume with two identical hulls.

meshes with a high resolution are adopted in the moonpool to account for the boundary layer effects and to accurately capture the large-amplitude free surface oscillation. In the outlet relaxation zone, the rectangular coarse meshes with a large aspect ratio up to 1/20 (height/length) are adopted, which are helpful to dissipate the reflection wave. The rectangular meshes with a medium resolution are utilized in the regions of the inlet relaxation zone and incident wave path. Tab. 1 represents the detailed schemes of convergence tests for four types of meshes, where the superscripts 'w' and 'mp' are defined as the meshes in the wave propagation path and inside the moonpool, respectively. A typical mesh scheme around the hulls is illustrated in Fig. 2, which is Mesh 3 in Tab. 1.

Table 1: Detailed information of four different mesh schemes for the mesh convergence study.

Parameters	Physical meaning	Mesh 1	Mesh 2	Mesh 3	Mesh 4
N_x^w	No. of cells per wave length λ	87	109	130	151
N_y^w	No. of cells along box height B_H	71	82	102	112
δy_{min}^w	Minimal cell height on free surface (mm)	5.33	4.21	3.47	3.07
N_x^{mp}	No. of cells along moonpool breadth B_{mp}	45	58	68	78
N_y^{mp}	No. of cells along box height B_H	120	150	180	210
δy_{min}^{mp}	Minimal cell height on free surface (mm)	1.25	1.00	0.83	0.71
	Total number of cells for the case	159985	244358	363712	458362

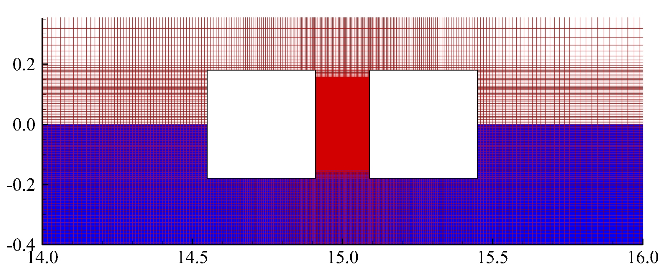

Figure 2: Typical grid system in this study around the hulls.

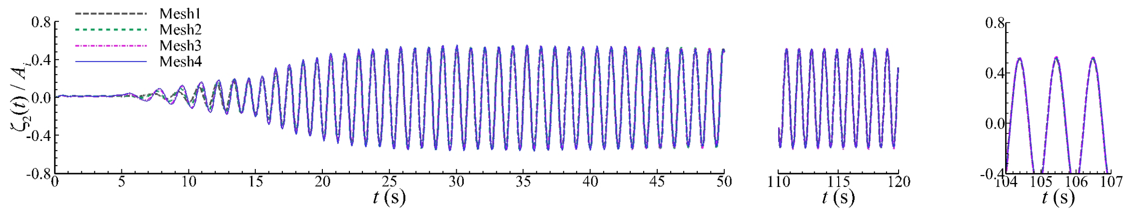

(a)

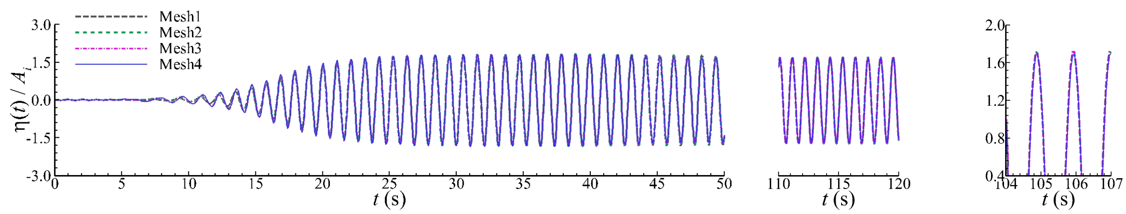

(b)

Figure 3: Mesh convergent tests for the evolutions of heave motion response of twin hulls and free surface oscillation in the moonpool. (a) Heave motion response, (b) Free surface oscillation.

Fig. 3 shows the evolutions of the heave motion response $\zeta_2(t)$ of the hulls and the free surface oscillation $\eta(t)$ in the moonpool, where the incident wave frequency $\omega = 6.00$ rad/s is selected. After a short transient period, the steady-state evolutions can be observed after $t = 25$ s, implying that the inlet and outlet zones have a satisfactory performance in generating and eliminating the incident and transmission waves, respectively. Numerical simulations also indicate that there is very little discrepancy between the steady-state results of Mesh 3 and Mesh 4, implying that the convergent solutions can be produced by Mesh 3.

Numerical results for the amplitudes of the heave motion response $\zeta_2(t)$ of twin hulls and the free surface oscillation $\eta(t)$ in the moonpool, that is, ξ_2 and A_{mp}, at four different wave frequencies are shown in Fig. 4. In the figure, the amplitudes ξ_2 and A_{mp} are calculated according to the averaged values of $\zeta_2(t)$ and $\eta(t)$ between 80 - 120 s, respectively. The comparisons show that the variation of mesh density has little effect on the amplitudes of heave motion and free surface when the number of cells exceeds 3×10^5. Again, Mesh 3 is able to produce convergent solutions, and hence it is adopted as the baseline for the following numerical analysis.

The numerical accuracy of the present turbulence model is validated against the experimental data in Faltinsen et al. (2007) for the twin hulls with sharp edge profiles, firstly. For the purpose of comparison, the potential flow solutions are also included in the figure. The twin hulls undergoing synchronous heave oscillations are adopted in Faltinsen et al. (2007), where the geometries of the hulls and moonpool are the same as the present setup in the convergent tests. Correspondingly, the left inlet relaxation zone is replaced with an outlet relaxation zone, by which the process in the laboratory tests in Faltinsen et al. (2007) can be simulated, correctly. Two forced heave amplitudes, A_b= 2.5 mm and 5.0 mm, are selected, and the values at the wave gauges G1 and G4 (700 mm from the right side of Hull B) are measured. Fig. 5 shows the variations

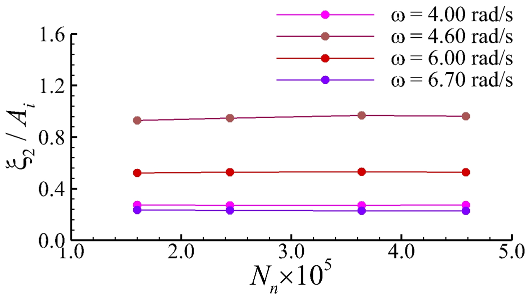

(a)

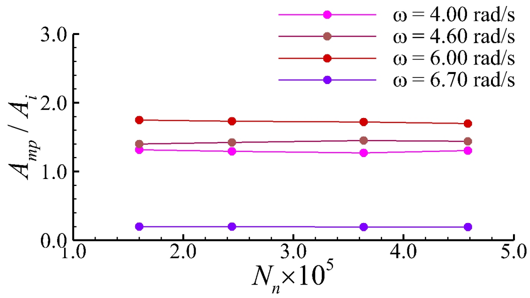

(b)

Figure 4: Mesh convergent tests for the amplitudes of heave motion response of twin hulls and free surface oscillation in the moonpool. (a) Heave motion response, (b) Free surface oscillation.

of wave amplitudes and phase shifts at G1 and G4 with the heave frequency $\omega^2 B_{mp}/g$. The potential flow model over-predicts the free surface amplitudes around the resonant frequency, which is attributed to neglecting the fluid viscosity and flow rotation. A good agreement between the present RNG results and the experimental data can be observed, for both the wave amplitudes and the phase shifts.

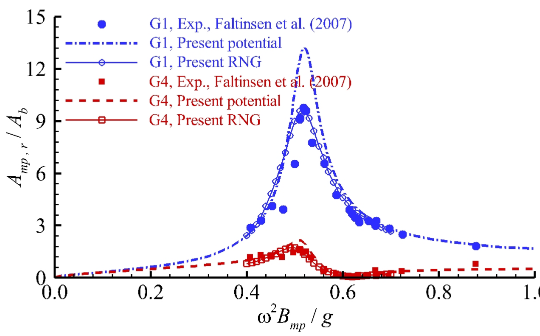

(a)

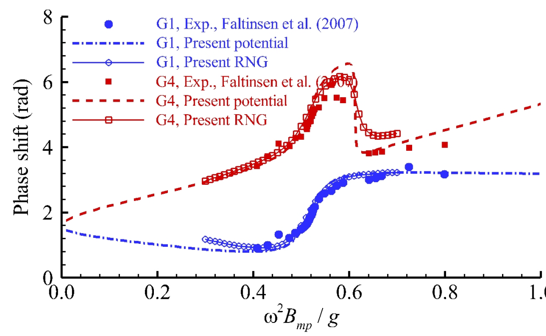

(b)

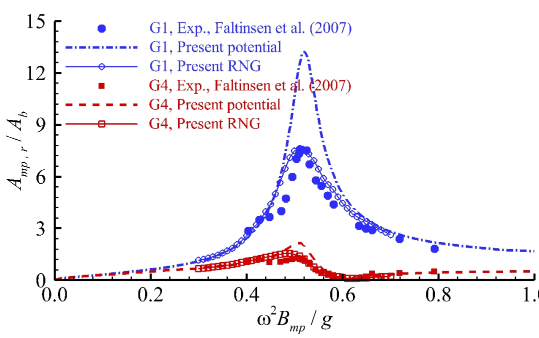

(c)

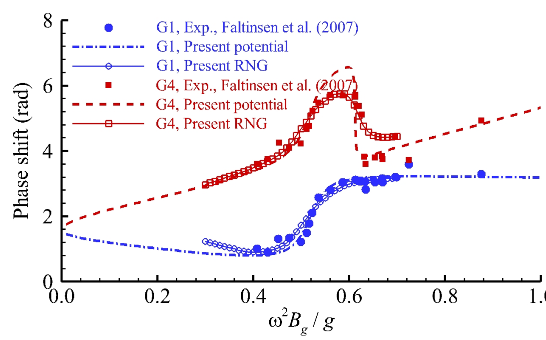

(d)

Figure 5: Numerical validation of the wave amplitudes and phase shifts at G1 and G4 versus the heave frequency for twin hulls under the heave amplitudes $A_b = 2.5$ mm and 5.0 mm. (a) Amplitude, $A_b = 2.5$ mm, (b) Phase shift, $A_b = 2.5$ mm, (c) Phase shift, $A_b = 2.5$ mm, (d) Phase shift, $A_b = 5.0$ mm.

To further validate the heave motion response of twin hulls and the free surface oscillation in the moonpool, another physical experiment in a wave flume with the water depth $h = 1.0$ m in Fredriksen et al. (2015) is simulated, where the twin hulls have the breadth $B_L = 0.201$ m and height $B_H = 0.201$ m and the moonpool has the draft $D = 0.097$ m and breadth $B_{mp} = 0.100$ m. The incident wave is given in the form of a wave steepness in their work, where two sets of wave steepness, $A_i/\lambda = 1/120$ and $1/90$, are selected in the present study. In the experiments, only the heave motion of the twin hulls is free, which means there is coupling actions between the heave motion of the hulls and the fluid resonance in the moonpool. Again, the potential flow solutions are included in the figure for the purpose of comparison. As shown in Fig. 6, the over-prediction can be observed in the potential flow solutions in the regions of $T = 7.5$ - 0.80 s and 0.9 - 1.1 s, respectively, for both the free surface and the heave motion amplitudes. The present viscous fluid flow model can work well in predicting the heave motion response and the free surface oscillation, which are in good agreement with the experimental measurement. According to the comparisons, it can be confirmed that the present viscous numerical wave flume is reliable for simulating the coupling actions between the heave motion and the fluid oscillation in the moonpool.

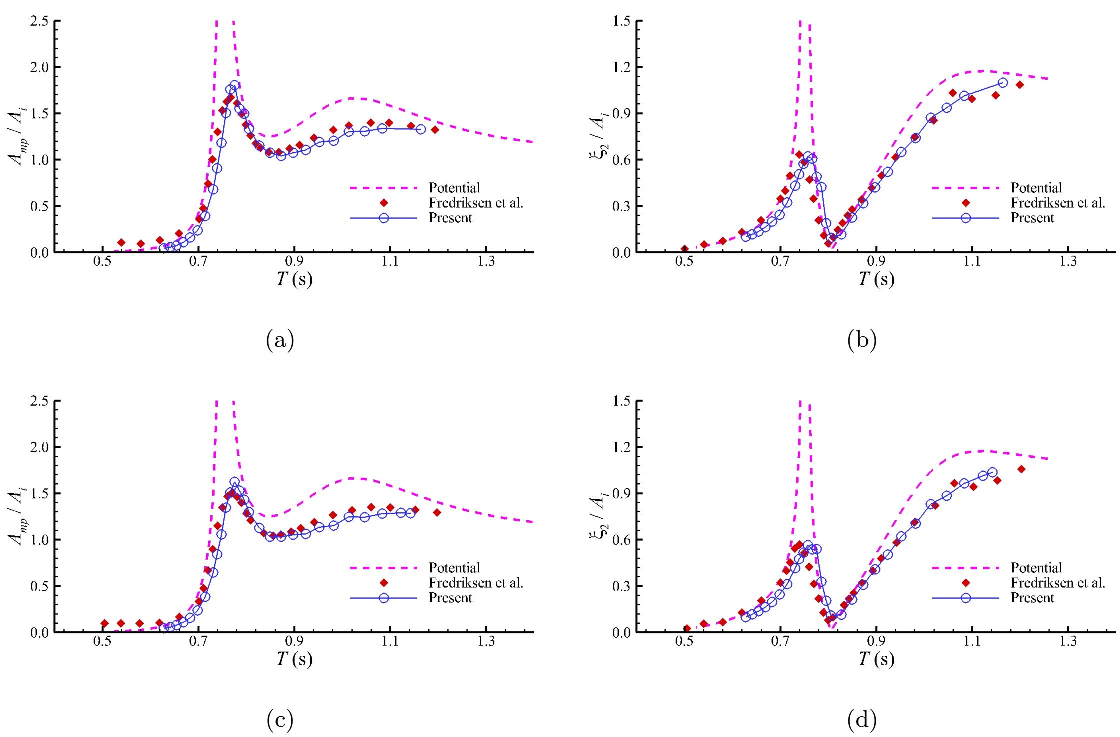

Figure 6: Numerical validation of the amplitudes of heave motion response of twin hulls and free surface oscillation in the moonpool. (a) $A_i/\lambda = 1$ / 120, A_{mp}/A_i, (b) $A_i/\lambda = 1$ / 120, ξ/A_i, (c) $A_i/\lambda = 1$ / 90, A_{mp}/A_i, (d) $A_i/\lambda = 1$ / 90, ξ/A_i.

4. Behavior of free surface oscillation and heave motion response

The motivation of this study is the coupling actions between the free surface oscillation in the moonpool and the heave motion response of twin hulls with the vertical mooring stiffness. The geometries adopted in the mesh convergent test, that is, the twin hulls with the breadth B_L = 0.360 m and height B_H = 0.360 m, and the moonpool with the breadth B_{mp} = 0.180 m and draft D = 0.180 m, in the water depth h = 1.030 m, are selected. The twin hulls are rigidly connected and only the heave motion is free. Six types of vertical stiffness, k = 0, 1000, 4000, 7000, 14000 and ∞, are selected, where the unit of stiffness is N/m. Note that the cases of $k = 0$ and $k = \infty$ correspond to the no-stiffness hulls and fixed hulls, respectively. The twin hulls are restricted to be free only in the z-axis direction, that is, only the heave direction is free. The potential flow model and viscous fluid flow model are adopted in the numerical simulations, where a wide range of incident wave frequencies from ω = 3.50 - 9.50 rad/s are considered. The incident wave height is H_i = 0.03 m in the viscous fluid flow simulations.

Fig. 7 shows the variation of the free surface oscillation A_{mp}/A_i in the moonpool and the heave motion response ξ_2/A_i of the hulls against the incident wave frequency, including the influence of the vertical mooring stiffness k. The potential flow model can firstly manifest a general impression of the behavior of the heave motion response and the free surface oscillation. As illustrated in Fig. 7a, the free surface amplitudes in the moonpool show the two-peak variation with the incident wave frequency for the cases of non-fixed twin hulls. One of the peaks is smooth and bounded at the low frequency range, which is defined as the first peak frequency $\omega_p^{(1)}$; while the other is a sharp spike at the high frequency range, which is defined as the second peak frequency $\omega_p^{(2)}$. The values of these two peak frequencies $\omega_p^{(1)}$ and $\omega_p^{(2)}$ increase with the increase of the vertical stiffness k, where the cases with $k = 0$ and $k = \infty$ are the two limitation cases. In the present geometry, the range of the first peak frequency $\omega_p^{(1)}$ is from 4.55 rad/s to 5.30 rad/s; while the range of the second peak frequency $\omega_p^{(2)}$ is from 6.15 rad/s to ∞. This implies that the frequency range between ω = 5.30 rad/s and 6.15 rad/s has no resonant frequency for any vertical stiffness. It should be noted that there is also no resonant frequency during the same range in the viscous fluid flow results in Fig. 7a, indicating that it may be a real physics for the moored twin hulls with the moonpool system.

The variation of the heave motion response with the incident wave frequency is illustrated in Fig. 7b, where only the single-peak value can be observed around the second peak frequency $\omega_p^{(2)}$. The comparison between Figs. 7a and 7b shows that the values of the second peak frequencies $\omega_p^{(2)}$ for the fluid resonance and the heave motion response are the same. At the first peak frequency $\omega_p^{(1)}$, the heave motion has no peak values, implying that the large-amplitude free surface oscillation in the moonpool has little effect on the heave motion response of the hulls. Another interesting phenomenon in Fig. 7b is the zero-amplitude heave motion response around the incident frequency ω = 5.76 rad/s. This is due to the fact that the vertical wave exciting force approaches zero, where the ratio of wavelength and twin-hull breadth is $\lambda/(2B_L + B_{mp})$ = 2.08. It can be understood that the vertical wave forces generated by the wave crest and wave trough are generally cancelled with each other at this frequency.

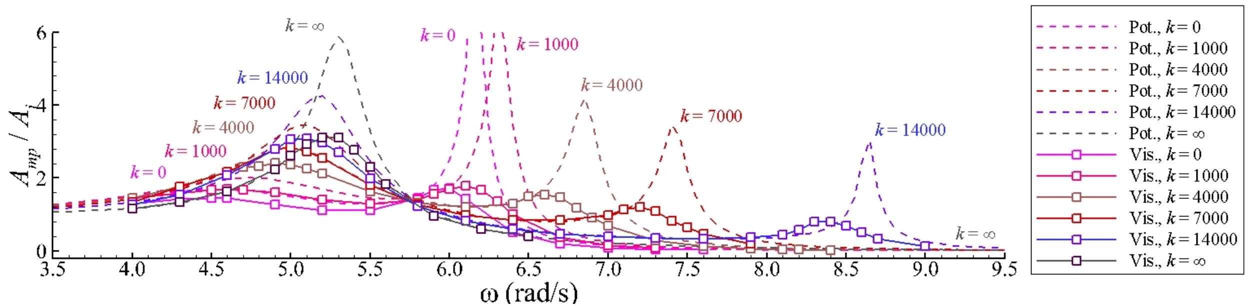

(a)

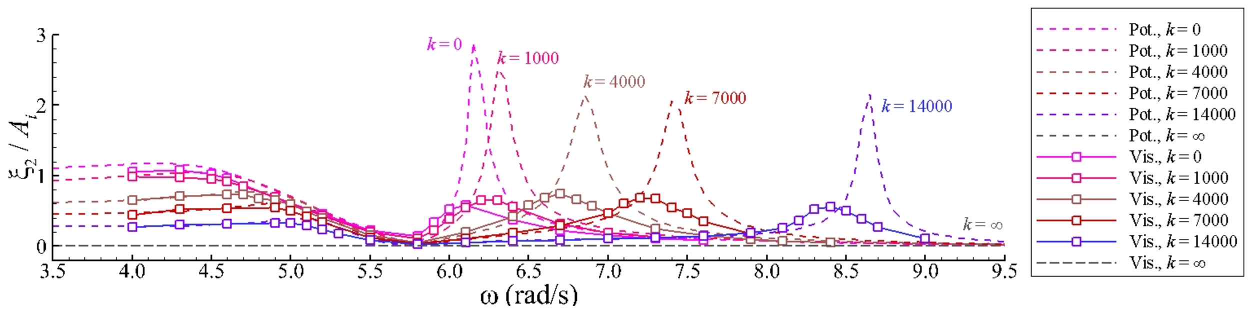

(b)

Figure 7: Variation of heave motion response and free surface oscillation against the incident wave frequency with different vertical mooring stiffnesses. (a) Free surface oscillation, (b) Heave motion response.

The potential flow model can only manifest a general understanding of the behavior of the free surface oscillation in the moonpool and the heave motion response of the hulls, while the real physical phenomena should be simulated by the viscous fluid flow model, especially around the two-peak frequencies $\omega_p^{(1)}$ and $\omega_p^{(2)}$. As shown in Fig. 7a, the potential flow model over-predicts the free surface amplitudes in the moonpool at the first and second peak frequencies $\omega_p^{(1)}$ and $\omega_p^{(2)}$. The over-prediction can also be found in the results of heave motion amplitudes around the second peak frequency $\omega_p^{(2)}$, as illustrated in Fig. 7b. All of these phenomena can be explained by the ignorance of the energy dissipation associated with the fluid viscosity and flow rotation. Oppositely, a little discrepancy of the heave motion amplitudes between two numerical models can be identified around the first peak frequency $\omega_p^{(1)}$ in Fig. 7b, implying that the energy dissipation effect is not very significant on the occasion.

Furthermore, the influence of the vertical stiffness on the potential flow and viscous fluid flow results are identified in Fig. 7. Around the first peak frequency $\omega_p^{(1)}$, the increased discrepancy of the free surface amplitudes between two numerical results can be observed with the increase of vertical stiffness. It indicates that the increase of vertical stiffness is able to generate more significant energy dissipation around the first peak frequency $\omega_p^{(1)}$. The influence of the vertical stiffness on the peak frequencies between two numerical models can also be reflected in the figure. That is, the increased vertical stiffness is able to increase the difference of the $\omega_p^{(1)}$ and $\omega_p^{(2)}$ values between the potential flow and viscous fluid flow results.

Fig. 8 shows the influence of incident wave amplitude at different vertical stiffnesses, where the normalized amplitudes of free surface oscillation A_{mp}/A_i in the moonpool and heave motion response of the twin hulls ξ_2/A_i are presented. A general description of the decreased normalized amplitudes A_{mp}/A_i and ξ_2/A_i with the increase of incident wave amplitude can be observed, which also deviates more from the potential flow solutions. It implies the increased influence of the energy dissipation associated with the fluid viscosity and flow rotation. Furthermore, the influence of the vertical stiffness on the variation of normalized values of A_{mp}/A_i and ξ_2/A_i is quantified in Tabs. 2 and 3, which are the ratio of the normalized amplitudes and the incident wave heights $H_i = 0.03$ m and 0.06 m at the first and second peak frequencies, respectively. The decreased ratio can be observed at the first peak frequency $\omega_p^{(1)}$ with the increase of vertical stiffness in Tab. 2, for both the normalized free surface amplitudes and the heave motion amplitudes. It demonstrates the increased influence of the energy dissipation at the first peak frequency $\omega_p^{(1)}$ with the increase of vertical stiffness. However, there is no simple regular pattern in the ratios at the second peak frequency $\omega_p^{(2)}$. Numerical results show the ratio values at the second peak frequency are always around about 60% - 70% in Tab. 3. It, in fact, implies that the energy dissipation plays a different role in the behavior of the free surface oscillation and heave motion response under different vertical stiffnesses, which will be further discussed in Sec. 5.

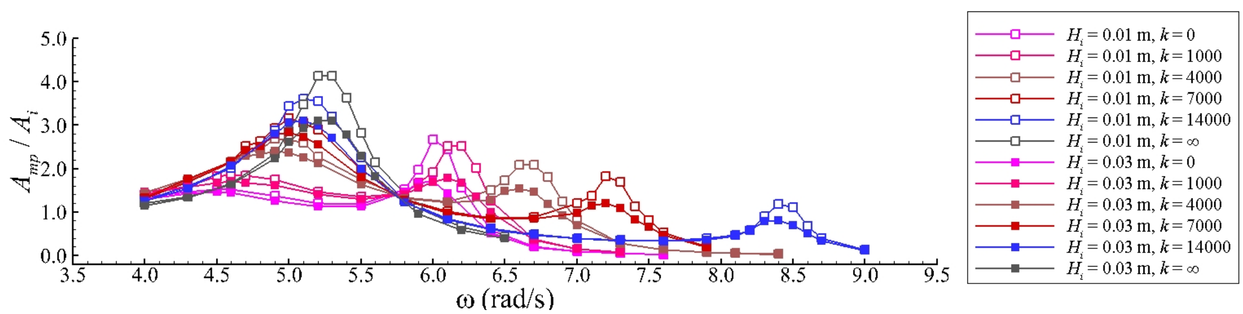

(a)

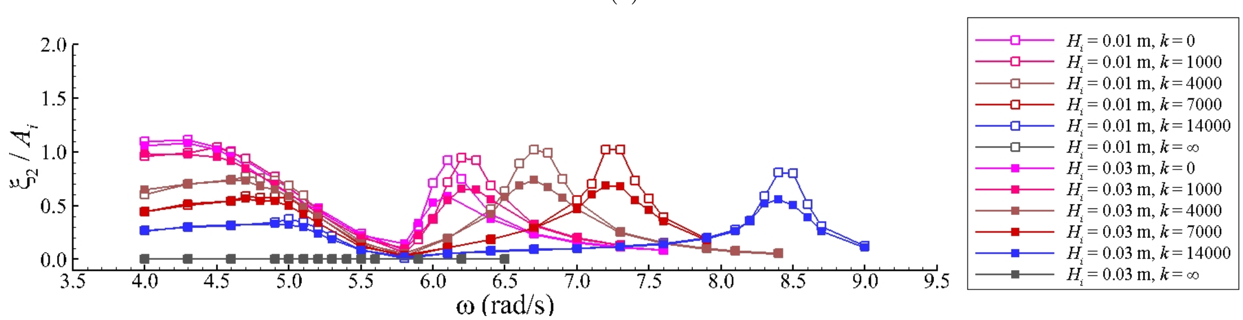

(b)

Figure 8: Variation of heave motion response and free surface oscillations against the incident wave amplitude with different vertical mooring stiffnesses. (a) Free surface oscillation, (b) Heave motion response.

Table 2: Normalized amplitudes of free surface oscillations A_{mp}/A_i and heave motion responses ξ/A_i under different incident wave heights at the first peak frequency $\omega_p^{(1)}$.

Parameters		$K=0$	$K=1000$	$K=4000$	$K=7000$	$K=14000$	$K=\infty$
A_{mp}/A_i	$H_i = 0.01$ m	1.530	1.862	2.680	3.166	3.606	4.134
	$H_i = 0.03$ m	1.459	1.701	2.405	2.835	3.096	3.107
	Ratio*	95.36%	91.35%	89.76%	89.56%	85.84%	75.15%
ξ_2/A_i	$H_i = 0.01$ m	1.040	0.998	0.729	0.570	0.345	0.000
	$H_i = 0.03$ m	1.020	0.914	0.647	0.496	0.296	0.000
	Ratio	98.06%	91.57%	88.72%	86.99%	85.89%	—

* Ratio means the ratio of the result at $H_i = 0.03$ m and the result at $H_i = 0.01$ m.

Table 3: Normalized amplitudes of free surface oscillations A_{mp}/A_i and heave motion responses ξ/A_i under different incident wave heights at the second peak frequency $\omega_p^{(2)}$.

Parameters		$K=0$	$K=1000$	$K=4000$	$K=7000$	$K=14000$	$K=\infty$
A_{mp}/A_i	$H_i = 0.01$ m	2.660	2.520	2.087	1.826	1.182	—
	$H_i = 0.03$ m	1.718	1.777	1.533	1.207	0.805	—
	Ratio	64.58%	70.53%	73.43%	66.09%	68.11%	—
ξ_2/A_i	$H_i = 0.01$ m	0.712	0.714	0.892	1.022	0.811	0.000
	$H_i = 0.03$ m	0.529	0.551	0.688	0.690	0.561	0.000
	Ratio	74.29%	77.20%	77.22%	67.51%	69.11%	—

5. Keulegan-Carpenter Number

Numerical simulations in Sec. 4 described the general behavior of the fluid resonance and heave motion response with different vertical stiffnesses, where the two-peak variation is the most important behavior for the twin-box with the moonpool system. To better understand the essential mechanism behind the phenomena, the detailed characteristics of the free surface oscillation and heave motion response are further discussed in this section. Figs. 9 and 10 show the time histories of the free surface elevation in the moonpool and the heave motion response of the hulls, where the first and second peak frequencies $\omega_p^{(1)}$ and $\omega_p^{(2)}$ with the vertical stiffnesses $k = 0$ and $k = 7000$ N/m are selected. As shown in Fig. 9, the free surface oscillation and heave motion response have the in-phase relationship at the first peak frequency $\omega_p^{(1)}$. Further comparison indicates that the amplitudes of the free surface elevation and heave motion response at the first peak frequency $\omega_p^{(1)}$ are very close when the vertical stiffness is $k = 0$; while the heave motion amplitude is evidently smaller than the free surface amplitude when the vertical stiffness is $k = 7000$ N/m. As for the second peak frequency $\omega_p^{(2)}$

in Fig. 10, the out-of-phase relationship can be observed between the free surface oscillation and the heave motion response for both $k = 0$ and 7000 N/m. The above in-phase and out-of-phase relationships at the first and second peak frequencies are also applicable to other vertical stiffnesses, which has been confirmed according to the careful examinations of the CFD simulations.

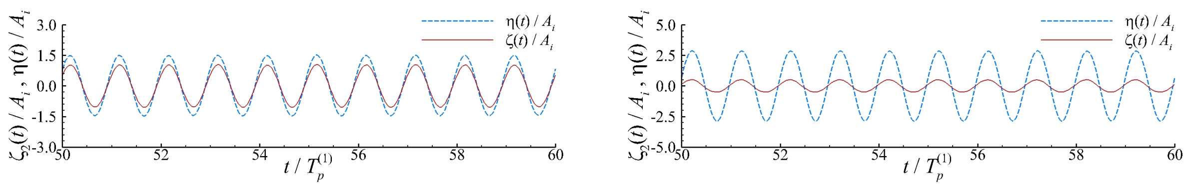

(a) (b)

Figure 9: Time histories of heave motion responses and free surface oscillations with $k = 0$ and $k = 7000$ N/m at the first peak frequency $\omega_p^{(1)}$. (a) $k = 0$, $\omega_p^{(1)} = 4.50$ rad/s, (b) $k = 7000$ N/m, $\omega_p^{(1)} = 5.00$ rad/s.

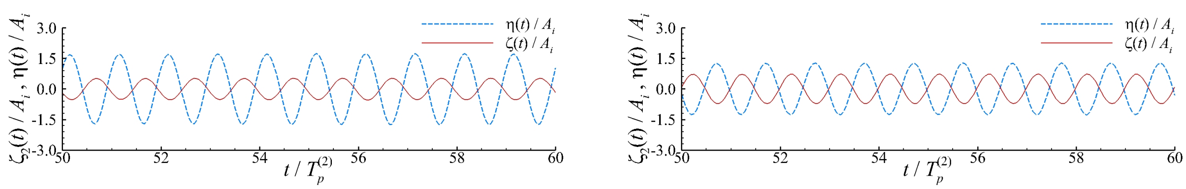

(a) (b)

Figure 10: Time histories of heave motion responses and free surface oscillations with $k = 0$ and $k = 7000$ N/m at the second peak frequency $\omega_p^{(2)}$. (a) $k = 0$, $\omega_p^{(2)} = 6.00$ rad/s, (b) $k = 7000$ N/m, $\omega_p^{(2)} = 7.20$ rad/s.

Moreover, a local Keulegan-Carpenter (KC) Number is defined as,

$$KC = V_A T / D, \tag{8}$$

where V_A is the amplitude of the averaged relative vertical fluid velocity along the moonpool bottom. T is the period of free surface oscillation in moonpool and D is the draft of the hulls. It is the relative velocity between the fluid motion and the heave response. The relative time-dependent space-averaged vertical velocity $\tilde{v}(t)$ can be computed as follows,

$$\tilde{v}(t) = \frac{1}{x_l - x_r} \int_{x_l}^{x_r} v(x,t)\, dx - \dot{\zeta}_2(t). \tag{9}$$

where $\dot{\zeta}_2(t)$ is the vertical velocity of the hulls, $v(x,t)$ is the time- and space-dependent vertical velocity in the space-fixed coordinate system along the horizontal entrance of the moonpool, and x_l and x_r are the left and right edges of the moonpool entrance attached to the twin hulls. In this work, V_A is calculated according to the averaged value of $\tilde{v}(t)$ between 80 s - 120 s, which is in accordance with the calculation of the free surface amplitude A_{mp} and the heave motion amplitude ξ_2 in Sec. 4.

The calculated KC Numbers at the first and second peak frequencies are illustrated in Tabs. 4 and 5, for two sets of incident wave heights and six types of vertical stiffness. For the purpose of comparison, the values of the free surface amplitude A_{mp}/A_i and the heave motion amplitude ξ_2/A_i at the first and second peak frequencies $\omega_p^{(1)}$ and $\omega_p^{(2)}$ with various vertical stiffnesses k from 0 to ∞ are also included in these tables. For a specific vertical stiffness, the values of KC Number at the incident wave height $H_i = 0.03$ m are always larger than those at $H_i = 0.01$ m at both the first and second peak frequencies $\omega_p^{(1)}$ and $\omega_p^{(2)}$. This confirms the increased influence of the fluid viscosity and flow rotation with the increase of the incident wave amplitude. It is the essential reason for the decreased normalized amplitudes of the free surface oscillation and heave motion response around the first and second peak frequencies in Fig. 8, where the viscous fluid flow results deviate more from the potential flow solutions with the increase of the incident wave amplitude.

Moreover, the influence of the vertical stiffness on the KC number can be quantified in these tables. As shown in Tab. 4, the KC number increases with the increase of the vertical stiffness at the first peak frequency $\omega_p^{(1)}$, indicating the energy dissipation plays a more important role. This is in accordance with the increased discrepancy between the potential flow and viscous fluid flow results with the increase of the vertical stiffness at the first peak frequency $\omega_p^{(1)}$ in Fig. 7. In fact, the above variation of the KC number can also be speculated based on Eq. (9) and Figs. 9 and 10. That is, the values of $v(x,t)$ and $\dot{\zeta}_2(t)$ always have the same sign due to the in-phase relationship at the first peak frequencies. On the occasion, the increase of the vertical stiffness would increase the relative motion V_A between the heave motion response and the free surface oscillation, leading to the increased KC number at the first peak frequency. Oppositely, as illustrated in Tab. 5, the KC number roughly decreases with the increase of the vertical stiffness at the second peak frequency $\omega_p^{(2)}$. The values of $v(x,t)$ and $\dot{\zeta}_2(t)$ always have the opposite sign because of the out-of-phase relationship at the second peak frequency. However, it is not a strict decrease in the KC number at the second peak frequency, which is attributed to the complex variation of the free surface oscillations in the moonpool with the vertical stiffness.

Finally, the KC numbers with various vertical stiffnesses at the first and second peak frequencies are compared. It can be observed that the effect of the vertical stiffness affects the KC number more significantly at the first peak frequency $\omega_p^{(1)}$ than that at the second peak frequency $\omega_p^{(2)}$. As an example, when the incident wave amplitude is $H_i = 0.03$ m, the KC number is from 0.460 to 3.253 with the increase of the vertical stiffness from $k = 0$ to $k = 14000$ N/m at the first peak frequency; while it ranges from 2.353 to 1.430 at the second peak frequency. In Tab. 4, the values of A_{mp}/A_i and ξ_2/A_i increase and decrease with the increase of the vertical stiffness at the first peak frequency. Based on Eq. (9) and the in-phase relationship, it is found that the variation of KC number comes from the contribution of both A_{mp}/A_i and ξ_2/A_i. At the second peak frequency, although the decreased values of A_{mp}/A_i can be observed, the insensitivity of ξ_2/A_i with the vertical stiffness appears in Tab. 5. It indicates the variation of KC number is only due to the change of A_{mp}/A_i. The above analysis also indicates that the energy dissipation plays a more important role with the increase of the vertical stiffness at the first peak frequency; while the influence of the vertical stiffness on the energy dissipation is not very sensitive at the second peak frequency.

Table 4: Variation of KC Number with the vertical mooring stiffness under two sets of incident wave heights at the first peak frequency $\omega_p^{(1)}$.

Parameters		$K = 0$	$K = 1000$	$K = 4000$	$K = 7000$	$K = 14000$	$K = \infty$
$H_i = 0.01$ m	A_{mp}/A_i	1.530	1.862	2.680	3.166	3.606	4.134
	ξ_2/A_i	1.040	0.998	0.729	0.570	0.345	0.000
	KC Number	0.171	0.302	0.681	0.906	1.138	1.443
$H_i = 0.03$ m	A_{mp}/A_i	1.459	1.701	2.405	2.835	3.096	3.107
	ξ_2/A_i	1.020	0.914	0.647	0.496	0.296	0.000
	KC Number	0.460	0.824	1.842	2.450	2.932	3.253

Table 5: Variation of KC Number with the vertical mooring stiffness under two sets of incident wave heights at the second peak frequency $\omega_p^{(2)}$.

Parameters		$K = 0$	$K = 1000$	$K = 4000$	$K = 7000$	$K = 14000$	$K = \infty$
$H_i = 0.01$ m	A_{mp}/A_i	2.660	2.520	2.087	1.826	1.182	—
	ξ_2/A_i	0.712	0.714	0.892	1.022	0.811	0.000
	KC Number	1.177	1.129	1.040	0.994	0.696	—
$H_i = 0.03$ m	A_{mp}/A_i	1.718	1.777	1.533	1.207	0.805	—
	ξ_2/A_i	0.529	0.551	0.688	0.690	0.561	0.000
	KC Number	2.353	2.439	2.326	1.987	1.430	—

6. Flow pattern analysis

The flow pattern in the vicinity of the moonpool is investigated for demonstrating the hydrodynamic behavior involved in the fluid resonance, as illustrated in Figs. 11 and 12 (Multimedia available online). The above geometry with the vertical stiffness $k = 0$ and 7000 N/m under the incident wave height $H_i = 0.03$ m at the corresponding first and second peak frequencies are selected. The vortex contours at eight time instants during a stable period T beginning from the up zero-crossing point of the free surface oscillation in the moonpool are considered. It should be noted that the free surface oscillation in the moonpool and the heave motion response of the hulls are in-phase and out-of-phase at the first and second peak frequencies, respectively, as illustrated in Figs. 9 and 10. This would play an important role in understanding the behavior of flow patterns affected by the vertical stiffness at two peak frequencies.

Fig. 11 (Multimedia available online) shows the flow patterns at the first peak frequency $\omega_p^{(1)}$ with the vertical stiffness $k = 0$ and 7000 N/m, where the free surface oscillation and the heave motion response are

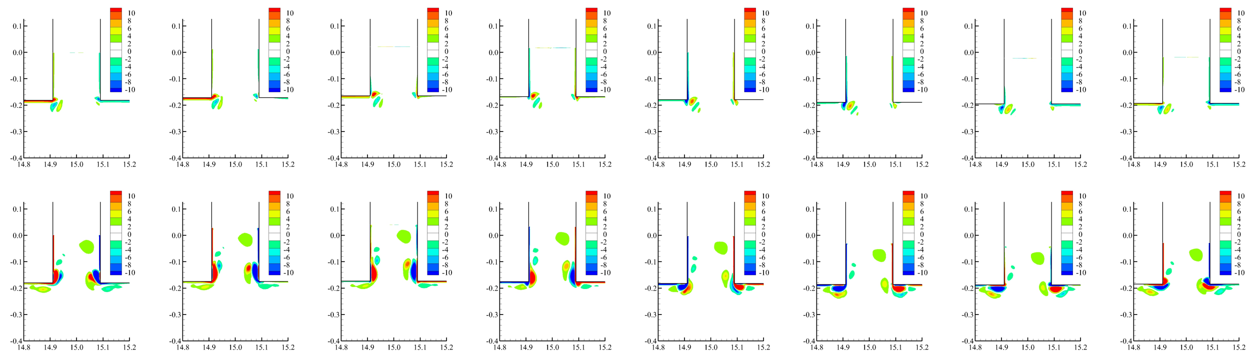

(a) (b) (c) (d) (e) (f) (g) (h)

Figure 11: Vortex contour in the near region of the moonpool entrance during one period of free surface oscillation at the first peak frequency. 1st row: $\omega = 4.50$ rad/s, $k = 0$; 2nd row: $\omega = 5.00$ rad/s, $k = 7000$. (a) 0, (b) $T/8$, (c) $2T/8$, (d) $3T/8$, (e) $4T/8$, (f) $5T/8$, (g) $6T/8$, (h) $7T/8$. (Multimedia available online)

in-phase. When the vertical stiffness is $k = 0$, the amplitudes of the free surface motion and heave motion response are very close. Correspondingly, the relative velocity between the fluid flow along the moonpool bottom and the heave motion of the hulls is very small. Therefore, it is hard to find the shear shedding and vortex structure in the first row of the figure. It implies the negligible influence of the energy dissipation on the hydrodynamic behavior of the moonpool resonance coupling with the heave motion response. In the second row of the figure, the relative velocity between the fluid flow and heave motion becomes large due to the effect of the vertical stiffness $k = 7000$ N/m. It can generate significant shear shedding and produce clear vortex structures, leading to the significant effect of energy dissipation. The above phenomena are essentially revealed by the KC number in Sec. 5, where the KC numbers increase with the increase of the vertical stiffness in Tab. 4. It also coincides with the results in Figs. 7 and 8, where the increased influence of the energy dissipation can be observed with the increase of the vertical stiffness at the first peak frequency.

Flow patterns at the second peak frequency $\omega_p^{(2)}$ with the vertical stiffness $k = 0$ and 7000 N/m are illustrated in Fig. 12 (Multimedia available online), where the free surface oscillation and the heave motion response are out-of-phase. The out-of-phase relationship means that the relative velocity between the fluid flow and the heave motion is always large at the frequency. Therefore, the evident shear shedding and clear vortex structures can be found in the first and second rows of the figures for both the vertical stiffness k = 0 and 7000 N/m. This implies that energy dissipation can always play an important role at the second peak frequency. In difference to the results at the first peak frequency, the influence of the vertical stiffness on the flow pattern is not very remarkable at the second peak frequency. This is in accordance with the conclusion that the variation of the KC number against the vertical stiffness at the second peak frequency $\omega_p^{(2)}$ is weaker than that at the first peak frequency $\omega_p^{(1)}$. According to the flow pattern analysis in Figs. 11 and 12 (Multimedia available online), it is confirmed that the conclusions about the local KC number are reasonable and supported by the physical mechanism.

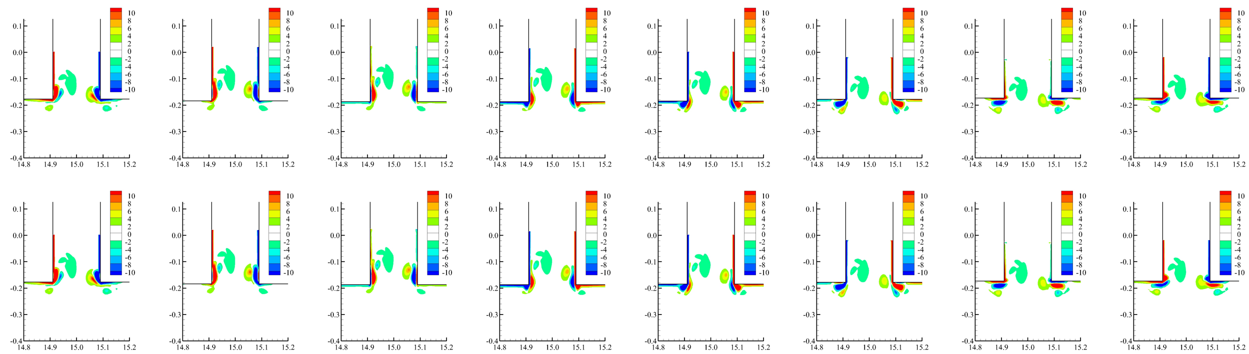

(a) 0 (b) $T/8$ (c) $2T/8$ (d) $3T/8$ (e) $4T/8$ (f) $5T/8$ (g) $6T/8$ (h) $7T/8$

Figure 12: Vortex contour in the near region of the moonpool entrance during one period of free surface oscillation at the second peak frequency. 1st row: $\omega = 6.00$ rad/s, $k = 0$; 2nd row: $\omega = 7.20$ rad/s, $k = 7000$. (a) 0, (b) $T/8$, (c) $2T/8$, (d) $3T/8$, (e) $4T/8$, (f) $5T/8$, (g) $6T/8$, (h) $7T/8$. (Multimedia available online)

7. Discussion

This study mainly focuses on the fundamental physics of coupling actions between the fluid resonance in the moonpool and the heave motion response of the hulls with vertical stiffness. The findings are potentially relevant to marine engineering applications. The vertical stiffness can significantly affect the two peak values of the heave responses and the free surface oscillations, including the peak amplitudes and peak frequencies. Around the two peak frequencies, the comparisons between the potential flow and viscous fluid flow models indicate that the influence of energy dissipation plays an important role. A local Keulegan-Carpenter (KC) number is defined for describing the energy dissipation effect on the fluid resonance and the heave motion response. The increase of the vertical stiffness can increase the KC number at the first peak frequency, indicating the increased effect of the energy dissipation with the increase of the vertical stiffness. At the second peak frequency, the variation of the KC number is not sensitive to the vertical stiffness, implying the influence of the energy dissipation is not much dependent on the vertical stiffness. The above quantitative analysis based on the local KC number is helpful in revealing the mechanism of energy dissipation in coupling actions.

In this study, numerical work is conducted in a two-dimensional domain, and only the piston-mode resonance and the heave motion response are discussed. The piston-mode features with free surface heaving up and down like a solid body, which has an important effect on heave motion responses, and a two-dimensional simulation is able to reveal the basic characteristics of the piston-mode resonance. However, there is another resonant mode, that is, sloshing-mode resonance in the moonpool, where the free surface is similar to the fluid motion inside a tank. It would cause more complex coupling actions with the motion response of the hulls. Therefore, a three-dimensional and six-degree-of-freedom work carried out in the future can generate more interesting information for practical engineering.

8. Conclusion

The highlight of this study is the coupling actions between the free surface oscillation in the moonpool and the heave motion response of the hulls with the vertical mooring stiffness. The free surface oscillation in the moonpool shows a two-peak variation with the incident wave frequency, which are defined as the first and second peak frequencies. However, only one peak value around the second peak frequency can be observed in the results of the heave motion response. The difference between the potential flow and viscous fluid flow results can be observed at the first and second peak frequencies. At the first peak frequency, the increase of the vertical stiffness is able to increase the difference between the two numerical models; while the insensitive variation of the difference with the vertical stiffness appears at the second peak frequency. The comparison of time histories shows that the free surface oscillation and heave motion response are in-phase and out-of-phase at the first and second peak frequencies, respectively, which plays an important role in understanding the influence of the vertical stiffness at two peak frequencies.

To better understand the essential mechanism behind the phenomena, a local Keulegan-Carpenter (KC) number is developed for quantifying the influence of the fluid viscosity and flow rotation. At the first peak frequency with the in-phase relationship, the increase of the vertical stiffness is able to increase the free surface oscillation and decrease the heave motion response, respectively. In addition, both the fluid motion and the heave motion are able to increase the KC number with the increase of the vertical stiffness. At the second peak frequency with the out-of-phase relationship, the increase of the vertical stiffness can increase the free surface amplitude but has little effect on the heave motion amplitude. Therefore, the influence of the vertical stiffness on the KC number at the second peak frequency is weaker than that at the first peak frequency. The above phenomena can be confirmed by the flow pattern analysis, where strong shear shedding and clear vortex structure can be observed in the cases with high KC numbers.

Declaration of competing interest

The authors declare that they have no known competing financial interests or personal relationships that could have appeared to influence the work reported in this paper.

Acknowledgments

This work is supported by the Natural Science Foundation of China with Grant Nos. 52371267 and 52171250. The first author gratefully acknowledges the Supercomputer Center of Dalian University of Technology for providing computing resources.

References

Chen, X. B. (2004). Hydrodynamics in offshore and naval applications - Part I, *Keynote lecture of 6th Intl. Conf. HydroDynamics, Perth, Australia.*

Faltinsen, O. M., Rognebakke, O. F. and Timokha, A. N. (2007). Two-dimensional resonant piston-like sloshing in a moonpool, *Journal of Fluid Mechanics* **575**: 359–397.

Feng, X. and Bai, W. (2015). Wave resonances in a narrow gap between two barges using fully nonlinear numerical simulation, *Applied Ocean Research* **50**: 119–129.

Feng, X., Chen, X. B. and Dias, F. (2018). A potential flow model with viscous dissipation based on a modified boundary element method, *Engineering Analysis with Boundary Elements* **97**: 1–15.

Fredriksen, A. G., Kristiansen, T. and Faltinsen, O. M. (2014). Experimental and numerical investigation of wave resonance in moonpools at low forward speed, *Applied Ocean Research* **47**: 28–46.

Fredriksen, A. G., Kristiansen, T. and Faltinsen, O. M. (2015). Wave-induced response of a floating two-dimensional body with a moonpool, *Philosophical Transactions of the Royal Society A: Mathematical, Physical and Engineering Sciences* **373**: 20140109.

Gao, J., He, Z., Huang, X., Liu, Q., Zang, J. and Wang, G. (2021). Effects of free heave motion on wave resonance inside a narrow gap between two boxes under wave actions, *Ocean Engineering* **224**: 108753.

Gao, J. L., Zang, J., Chen, L. F., Ding, H. Y. and Liu, Y. Y. (2019). On hydrodynamic characteristics of gap resonance between two fixed bodies in close proximity, *Ocean Engineering* **173**: 28–44.

Gao, J., Mi, C., Song, Z. and Liu, Y. (2024). Transient gap resonance between two closely-spaced boxes triggered by nonlinear focused wave groups, *Ocean Engineering* **305**: 117938.

Issa, R. I. (1986). Solution of the implicitly discretised fluid flow equations by operator-splitting, *Journal of Computational Physics* **62**(1): 40–65.

Iwata, H., Saitoh, T. and Miao, G. (2007). Fluid resonance in narrow gaps of very large floating structure composed of rectangular modules, *Proceedings of the Fourth International Conference on Asian and Pacific Coasts, Nanjing, China*, pp. 815–826.

Jacobsen, N. G., Fuhrman, D. R. and Fredsøe, J. (2012). A wave generation toolbox for the open-source cfd library: Openfoam®, *International Journal for Numerical Methods in Fluids* **70**: 1073–1088.

Jiang, S. C., Bai, W. and Tang, G. Q. (2018). Numerical simulation of wave resonance in the narrow gap between two non-identical boxes, *Ocean Engineering* **156**: 38–60.

Jiang, S. C., Tang, P., Zou, L. and Liu, Z. (2017). Numerical simulation of fluid resonance in a moonpool by twin rectangular hulls with various configurations and heaving amplitudes, *Journal of Ocean University of China* **16**(3): 422–436.

Jing, P., Cui, T., He, G., Zhang, C. and Luan, Z. (2024). Effects of multi motion responses and incident-wave height on the gap resonances in a moonpool, *Physics of Fluids* **36**(1).

Jing, P., He, G., Chen, B., Zhang, C. and Ng, B. (2023). Effects of roll motion on linear and nonlinear gap resonances in a moonpool excited by various incident-wave heights, *Physics of Fluids* **35**(10).

Li, S. and Teng, B. (2021). Fluid resonance between twin floating barges with roll motion under wave action, *China Ocean Engineering* **35**(6): 789–801.

Liu, Y. and Li, H.-J. (2014). A new semi-analytical solution for gap resonance between twin rectangular boxes, *Journal of Engineering for the Marine Environment* **228**(1): 3–16.

Lu, L., Cheng, L., Teng, B. and Zhao, M. (2010). Numerical investigation of fluid resonance in two narrow gaps of three identical rectangular structures, *Applied Ocean Research* **32**: 177–190.

Lu, L., Tan, L., Zhou, Z., Zhao, M. and Ikoma, T. (2020). Two-dimensional numerical study of gap resonance coupling with motions of floating body moored close to a bottom-mounted wall, *Physics of Fluids* **32**: 092101.

Lu, L., Teng, B., Cheng, L., Sun, L. and Chen, X. (2011a). Modelling of multi-bodies in close proximity under water waves-fluid resonance in narrow gaps, *Science China Physics, Mechanics and Astronomy* **54**(1): 16–25.

Lu, L., Teng, B., Sun, L. and Chen, B. (2011b). Modelling of multi-bodies in close proximity under water waves-fluid forces on floating bodies, *Ocean Engineering* **38**: 1403–1416.

Molin, B., Zhang, X., Huang, H. and Remy, F. (2018). On natural modes in moonpools and gaps in finite depth, *Journal of Fluid Mechanics* **840**: 530–554.

Moradi, N., Zhou, T. and Cheng, L. (2015). Effect of inlet configuration on wave resonance in the narrow gap of two fixed bodies in close proximity, *Ocean Engineering* **103**: 88–102.

Newman, J. (2004). Progress in wave load computations on offshore structures, *Invited Lecture, 23th OMAE Conference, Vancouver, Canada, http://www. wamit. com/publications.*

Ravinthrakumar, S., Kristiansen, T., Molin, B. and Ommani, B. (2020). Coupled vessel and moonpool responses in regular and irregular waves, *Applied Ocean Research* **96**: 102010.

Saitoh, T., Miao, G. and Ishida, H. (2006). Theoretical analysis on appearance condition of fluid resonance in a narrow gap between two modules of very large floating structure, *Proceedings of the Third Asia-Pacific Workshop on Marine Hydrodynamics, Shanghai, China*, pp. 170–175.

Sun, L., Eatock Taylor, R. and Taylor, P. H. (2010). First-and second-order analysis of resonant waves between adjacent barges, *Journal of Fluids and Structures* **26**: 954–978.

Tan, L., Cheng, L. and Ikoma, T. (2021). Damping of piston mode resonance between two fixed boxes, *Physics of Fluids* **33**(6): 062117.

Tan, L., Lu, L., Tang, G. Q., Cheng, L. and Chen, X. B. (2019). A viscous damping model for piston mode resonance, *Journal of Fluid Mechanics* **871**: 510–533.

Teng, B. and Eatock Taylor, R. (1995). New higher-order boundary element methods for wave diffraction/radiation, *Applied Ocean Research* **17**(2): 71–77.

Wang, H., Wolgamot, H., Draper, S., Zhao, W., Taylor, P. and Cheng, L. (2019). Resolving wave and laminar boundary layer scales for gap resonance problems, *Journal of Fluid Mechanics* **866**: 759–775.

Yakhot, V. and Orszag, S. A. (1986). Renormalization group analysis of turbulence. I. Basic theory, *Journal of Scientific Computing* **1**(1): 3–51.

Yakhot, V. and Smith, L. M. (1992). The renormalization group, the ε-expansion and derivation of turbulence models, *Journal of Scientific Computing* **7**(1): 35–61.

Zhang, C., Sun, X., Wang, P., Chen, L. and Ning, D. (2022). Hydrodynamics of a floating liquid-tank barge adjacent to fixed structure in beam waves, *Physics of Fluids* **34**(4).

Zhao, D.-y., Hu, Z.-q. and Chen, G. (2017b). Experimental investigation on dynamic responses of FLNG connection system during side-by-side offloading operation, *Ocean Engineering* **136**: 283–293.